






Cite this: *React. Chem. Eng.*, 2024, 9, 251

3D printed filtration and separation devices with integrated membranes and no post-printing assembly†

Molly J. Clark, ^{abc} Tushar Garg,^b Kathryn E. Rankin,^d Darren Bradshaw ^{ac} and Adrian M. Nightingale ^{*bc}

Additive manufacturing, or three-dimensional (3D) printing, is an accessible, quick, and user-friendly tool for fabricating reactors and chemical processing devices. Here we report a method for printing filtration and separation devices using fused-deposition modelling (FDM) which incorporate commercial porous membranes. By using exogenous membranes, membrane pore size and material can be arbitrarily specified allowing much greater versatility in device design. We show for the first time that fully operational monolithic devices can be created without need for post-printing assembly and demonstrate the efficacy of the approach by making and testing three distinct devices: dead-end filters, which can be made in a range of sizes and are shown to fully remove micron-sized particles from a heterogenous mixture; liquid-liquid separators, which are shown to completely separate segmented flows of immiscible liquids; and a cross-flow filtration device, which is shown to achieve near full dye removal from an aqueous stream with a residence time of 3.4 minutes. For the cross-flow filtration device we describe a new “double-sided” printing technique whereby the plastic is directly printed onto both sides of the membrane to ensure the membrane is fully bonded to the 3D printed body. The range of devices showcased here highlights the versatility of the approach and its potential for use in chemical processing applications that require porous membranes.

Received 24th April 2023,
Accepted 27th September 2023

DOI: 10.1039/d3re00245d

rsc.li/reaction-engineering

Additive manufacturing, or three-dimensional (3D) printing is a fabrication process that can directly create complex and bespoke parts from computer-aided design (CAD) files.¹ Typically used in manufacturing industries for rapid prototyping, it has recently seen significant traction for fabricating fluidic devices² with recent reports describing devices for synthesis,^{3,4} fluid mixing,⁵ dialysis,⁶ and analysis.^{1,7} Its continuing development within the flow chemistry and microfluidic communities, is highlighted by various recent reviews on the topic.^{1,2,8–11}

Several different methods have been used to make fluidic devices including stereolithographic^{12–14} and polyjet^{15,16} printing, however fused deposition modelling (FDM) is highly

attractive for its low cost, wide range of available materials, and the ease with which other elements (actuators, sensors *etc.*) can be incorporated to enable additional functionality.¹⁷ FDM printers create objects by extruding a thermoplastic through a nozzle moving in a two-dimensional plane, building up the 3D object layer by layer. At any point external materials can be easily incorporated using the “print-pause-print” (PPP) approach⁶ whereby the print is stopped, the external element is inserted into a pre-designed recess, and then printing resumed to encapsulate it. This enables fully functional, integrated devices to be fabricated with minimal intervention and no post-printing assembly. PPP has been demonstrated using polyjet⁶ and stereolithographic printers,¹⁸ however FDM allows a much greater range of materials, allowing extra functionality (*e.g.* using conductive or flexible materials) and/or high chemical compatibility (*e.g.* when printing with polypropylene or polyvinylidene difluoride) – essential for synthetic chemistry applications.

The PPP approach has been used to embed commercial objects such as stirrer bars,^{7,19} glass windows,^{20,21} electrodes,²⁰ sensors,²² LEDs,²³ circuits,^{23,24} and electromagnets²⁴ to increase the functionality of printed fluid devices. Incorporation of membranes is particularly interesting as these can be used for a range of different

^a Department of Chemistry, Faculty of Engineering and Physical Sciences, University of Southampton, Southampton, SO17 1BJ, UK

^b Department of Mechanical Engineering, Faculty of Engineering and Physical Sciences, University of Southampton, Southampton, SO17 1BJ, UK.

E-mail: a.nightingale@southampton.ac.uk

^c Centre of Excellence for Continuous Digital Chemical Engineering Science, Faculty of Engineering and Physical Sciences, University of Southampton, SO17 1BJ, UK

^d μ -VIS X-Ray Imaging Centre, Faculty of Engineering and Physical Sciences, University of Southampton, Southampton, SO17 1BJ, UK

† Electronic supplementary information (ESI) available. See DOI: <https://doi.org/10.1039/d3re00245d>



filtration^{25,26} and separation⁶ applications. Multi-material FDM printing has been used to print permeable barriers within devices using a secondary, porous material,²⁷ however there are only a handful of printable porous materials, in stark contrast to the huge range of membrane materials and pore sizes possible if incorporating commercial membranes using PPP. Polyjet printing has been used to develop membrane-based separation devices using PPP and commercial membranes^{6,25} however these required post-printing assembly – increasing the fabrication complexity and potential failure points. While a previous report has shown proof-of-principle that FDM printing can be used to incorporate commercially purchased membranes using PPP,²⁸ there have been no reports, to the best of our knowledge, describing fully functional devices incorporating membranes that do not require post-printing assembly.

In this report we show how the PPP technique can be used to integrate commercial membranes into monolithic FDM printed devices to make useful systems for filtration and separation. We demonstrate the versatility of the approach by producing three distinct devices that utilize the properties of the inserted membrane in three different ways: a dead-end filter (a syringe filter more specifically), a liquid–liquid separator, and a cross-flow filtration device. For the cross-flow filtration device we showcase a novel “double-sided” printing technique to ensure optimum adhesion between the membrane and the printed part. In each case the printing parameters are carefully controlled to ensure the devices are leak free, the membrane is sealed in place, and the final device operates as designed without need for any subsequent assembly. All device dimensions can be customized depending on user needs.

Experimental methods

Materials

Clear polypropylene filament (2.85 mm cross section diameter, Ultimaker brand) was obtained from RS. Membranes were purchased from Thermo Fisher (Whatman, mixed cellulose ester $\varnothing = 20$ mm, 30 mm, 125 mm; Fisherbrand, mixed cellulose ester and nylon, $\varnothing = 47$ mm); and VWR (Cytvia, nylon, $\varnothing = 90$ mm). Where 40 mm membranes were used, these were manually cut from larger filters. Zn(NO₃)₂·6H₂O (98%), 2-methyl imidazole (98%), methylene blue, and ethanol were purchased from Sigma Aldrich. Fluorinert FC-40 fluorinated oil was obtained from Acota Ltd UK. ZIF-8 was synthesised from zinc nitrate and 2-methyl imidazole through a simple one pot synthesis at room temperature in deionised water over 48 h using a zinc: imidazole molar ratio of 1:12, according to previous reports.²⁹

Device design and general fabrication protocol

All devices were designed using a combination of AutoCAD (Autodesk) and SOLIDWORKS (Dassault) software. All designs included inlet/outlets that incorporated threads for standard

1/8"-28 fittings so that they could be easily interfaced with external tubing. All designs featured a cavity for the membrane. The height of the cavity was 100 μm and the diameter was set to be 200 μm larger than that of the membrane. The 3D design files (.3mf) were prepared for printing using Cura (Ultimaker). They were printed using an Ultimaker 3 FDM printer in polypropylene (PP), with an Ultimaker adhesion sheet applied to the print bed to ensure adhesion. The default print parameters were as follows: layer height, 100 μm ; infill, 100%; print speed, 40 mm s⁻¹; flow rate, 110%; fan speed, 0%. Post-processing scripts were used in Cura to add a pause at a predefined point so that the membrane could be added. During this pause the membrane was inserted, with a small quantity of an all-purpose paper adhesive (UHU) lightly applied to the circumference to ensure it did not move when subsequent layers were printed on it. The next two layers after the print was resumed had altered print parameters (specified in the Cura software using the “ChangeatZ” function) to ensure the membrane was incorporated with a liquid-tight seal: a slower print speed (20 mm s⁻¹) and increased flow rate (150%). After these two layers, all remaining print layers were printed with the original print speed and flowrate (40 mm s⁻¹ and 110% respectively) until completion. Using the general protocol, a series of syringe filters ($\varnothing = 20$ mm, 30 mm, 40 mm) were fabricated using Whatman grade 1 membranes (mixed cellulose ester, pore size = 11 μm , $\varnothing = 20$ mm, 30 mm, 125 mm) and Fisherbrand membranes (nylon, pore size = 0.45 μm , $\varnothing = 47$ mm). Where 40 mm membranes were used, these were manually cut from larger filters. Separator devices incorporated Fisherbrand membranes (nylon and mixed cellulose ester, pore size = 0.45 μm , $\varnothing = 47$ mm) and the cross-flow filtration device incorporated a Cytvia membrane (nylon, pore size = 0.2 μm , $\varnothing = 90$ mm). Dimensions of individual devices and any changes to this default protocol are described in the results section. All 3D device design files are included in the ESI.†

Syringe filter testing

Preformed ZIF-8 particles were dispersed in DI water (30 mg, 5 mL) by sonication to yield a cloudy suspension. It was transferred to a syringe with a Luer lock. The 3D printed syringe filter was fitted and the syringe contents passed through it. The quantity of ZIF-8 in the resulting fluid was assessed *via* light transmission measurements using a UV-2700 Shimadzu spectrophotometer.

CT scanning

Micro-focus X-ray CT (μCT) scanning was used as a non-destructive analysis tool for volumetric assessment of the internal bond between the 3D printed housing and filter insert within a tested syringe filter. Using a 160 kVp Zeiss Xradia Versa 510 X-ray microscope CT scanner (Carl Zeiss Microscopy GmbH, Germany), the syringe filter was orientated in the sample holder assembly such that the inlet/



outlet ports were perpendicular to the axis of rotation and positioned with a source-to-object distance of 25 mm and an object-to-detector distance of 150 mm. A two-stage (low resolution /high resolution) scanning process was used to image a region of interest incorporating the boundary between the 3D print and the edge of the filter material.

For the low resolution scan (5.0 μm voxel size), the X-ray conditions were set to 110 kVp peak voltage and 10 W power, and the imaging configuration used the 0.4 \times objective (binning = 1) with a 6 s exposure time; 3201 projection images were acquired throughout 360 degrees rotation. All these parameters are summarised in the ESI,[†] along with corresponding parameters for the high resolution scan (2.5 μm voxel). Projection data was reconstructed into TXM files using the Zeiss XM Reconstructor software (Carl Zeiss Microscopy GmbH, Germany). These were subsequently converted to 16-bit raw volumes for visualisation in ImageJ.

Liquid–liquid separator testing

A segmented flow of aqueous/non-aqueous fluid (water/FC-40) was generated using a syringe pump (Harvard PHD2000) to drive each fluid through PTFE tubing (0.8 mm inner diameter) into a T-junction (Upchurch Scientific, P-712). The water was coloured with red food dye to aid visualisation. The T-junction outlet was connected to the 3D printed separator. Capillary tubing ($\varnothing = 0.56$ mm, $L = 0.5$ –7 m) was applied to the retentate outlet (*i.e.* the outlet on the same side of the membrane as the incoming fluid) to provide a pressure difference across the membrane, with the length of the capillary systematically varied to change the backpressure. The permeate fluid (fluid that had passed through the membrane) and retentate fluid were collected, weighed and used to determine the separation efficiency at various flow rates (0.1–0.3 mL min⁻¹).

Cross-flow filtration testing

A 0.01 mM methylene blue solution in water was made, collected in a syringe and loaded into a syringe pump. A syringe loaded with DI water was loaded into a second pump. The syringes were directly connected to the 3D printed device *via* PTFE tubing and 1/4"-28 fittings at opposing sides to give counter current flow above and below the membrane with outlet tubing directed to vials for fluid collection. A micrometering valve (IDEX Health and Science, Micro-ming, P-445) was applied to the top outlet stream to apply a manually adjusted back pressure. Equal flow rates were applied from each syringe (25–2000 $\mu\text{L min}^{-1}$). The system was allowed to equilibrate after each flow rate change, then periodic collection of the outlet fluid was taken and analysed *via* UV-vis absorption spectrometry (UV-2700, Shimadzu). The amount of dye removed from the process fluid and hence, the separator efficiency could then be quantified.

Results and discussion

Syringe filter

The simplest possible filtration device is a dead-end filter, where the fluid is driven through a filter membrane. Syringe filters – dead-end filters that can be attached to syringes *via* a Luer adaptor – were fabricated as shown in Fig. 1. The filter design (Fig. 1A) is shown in the orientation it was printed, with accompanying cross sections showing the fluidic channels (dark blue, height = 500 μm) immediately above and below the membrane. To ensure a watertight seal on the membrane after it was inserted, plastic was extruded with an increased flow rate (ensuring no gaps between the membrane and the 3D printed monolith) and a reduced print speed (ensuring the lateral movement of the printhead did not displace the membrane) as shown inset in Fig. 1A. A final printed filter using a 30 mm diameter membrane is shown in Fig. 1B with the incorporated Luer lock feature ensuring an easy leak-free fit to a Luer-tipped syringe.

To show the efficacy of the syringe filter, it was used to separate a heterogenous dispersion of ZIF-8 crystals (a prototypical Zn-imidazolate metal–organic framework) in water which featured particle sizes of 0.3 to 15.0 μm (Fig. 2A). While the starting dispersion (Fig. 2B left) was a cloudy white mixture, the resulting filtrate was optically clear (Fig. 2B right) indicating the solid material had been

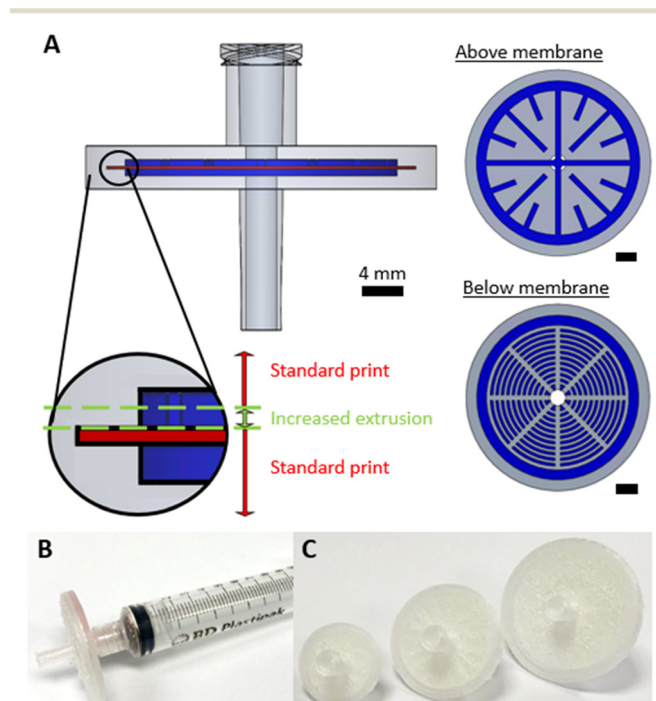


Fig. 1 A) Computer generated images showing the internal geometry of the syringe filter. The red area represents the membrane cavity, while blue areas represent the channel system above and below the membrane. All scale bars represent 4 mm. B) Image of a finished syringe filter (30 mm diameter membrane) attached to a syringe *via* the Luer fitting. C) Images of syringe filters of different size (membranes of 20, 30, and 40 mm diameter) showing how the design can be easily changed as required.



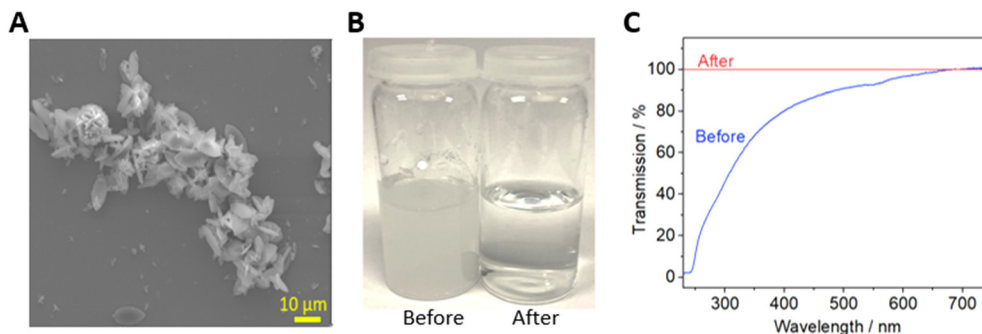


Fig. 2 A) SEM image of the metal organic framework particles within the sample that was filtered. B) Images of the suspension before and after a single pass through the 3D printed syringe filter. C) The corresponding optical transmission spectra.

successfully removed. This was confirmed by examining each solution by spectrophotometry (Fig. 2C). The cloudy dispersion prior to filtration reduced light transmission at low wavelengths due to scattering, while the filtrate showed no scattering effects – indicating good removal by the syringe filter in a single pass.

Anecdotally, we note that the plastic extruded directly onto the membrane forms a close conformal bond such that upon cooling, the membrane is physically attached to the extruded plastic as previously reported,³⁰ and that this bond did not notably differ with membrane material. To investigate the bond between the extruded material and membrane, μ CT was used to non-destructively image the internal structure of a used syringe filter (Fig. 3). The fibrous, intertwined structure of the membrane can be clearly seen attached to the upper side of the void at the places where plastic has been extruded directly onto the membrane (Fig. 3B and C). At the plastic/membrane interface there is close conformal contact (Fig. 3B) with the structured surface of the membrane, and occasional fibres are seen encapsulated within the plastic itself (e.g. highlighted in Fig. 3B by the red arrow). It is noteworthy that this bond is still present despite the syringe filter having been previously used, evidenced by the solid white MOF deposits remaining (Fig. 3C). A slight bowing of the membrane between the polypropylene contact points (e.g. Fig. 3C, right hand side) is consistent with the plastic shrinking slightly during cooling but maintaining a

firm bond with the membrane. Furthermore, these results preclude the idea that the membrane material is melted or otherwise compromised during extrusion.

The same protocol can be used to make various filters with different membrane materials (e.g. cellulose, mixed cellulose esters, nylon) and sizes (e.g. 20 mm, 30 mm, 40 mm, Fig. 1C) demonstrating the versatility of the approach. 3D printed syringe filters have been previously reported using stereolithographic & inkjet 3D printing,^{25,31} but this is the first 3D printed design printed from a single monolithic structure, meaning no manual assembly and hence fewer potential failure points.

Liquid–liquid separator

The same 3D printing technique was applied to the more complex problem of membrane-based devices for separating mixtures of immiscible fluids. Membrane-based separators are typically used for inline separation of fluids with similar densities which prohibit gravimetric separation, exploiting the differing wetting properties of immiscible fluids. Fig. 4A illustrates the operation of a membrane-based separator showing how an incoming stream of immiscible fluids (yellow and red) can be split into two single-phase streams. If the membrane is made of a hydrophilic material, a small applied trans-membrane pressure difference will drive the hydrophilic phase through the membrane pores (red, the

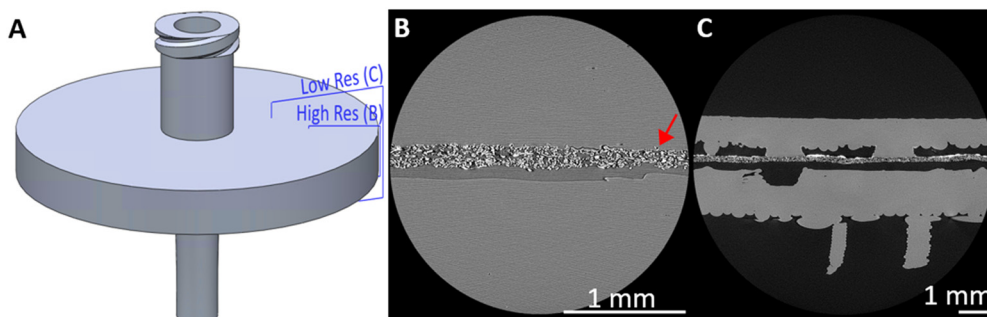


Fig. 3 A) CAD diagram with planes showing where CT images were taken from; B) a high resolution and C) low resolution CT scan showing the membrane conformally bonded to the extruded plastic on one side. The red arrow indicates a singular membrane fibre having been incorporated within the plastic.



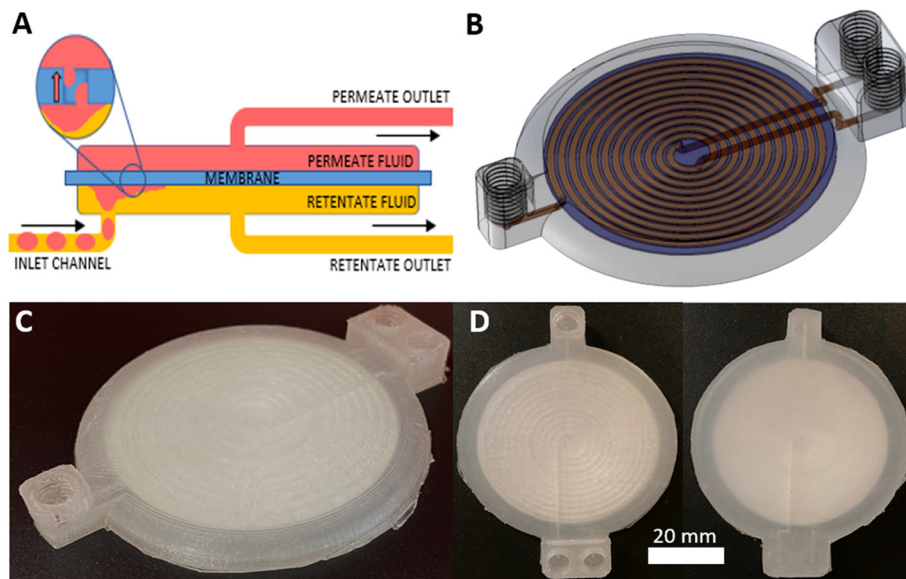


Fig. 4 A) Cartoon illustrating the liquid-liquid separation method B) 3D computer generated image showing the internal geometry of the separator, with the inlet on the left and outlets on the right. C) The corresponding view of a finished device. D) Views of the finished device from above and below, showing clearly how the two outlet channels come from different sides of the membrane.

“permeate” phase) but not the hydrophobic phase (yellow, “retentate” phase) due to its reduced affinity for the membrane and higher associated capillary pressure. Indeed the hydrophobic phase will not pass through the membrane as long as the pressure difference across the membrane is less than the total capillary pressure.^{32,33} The reverse behaviour (retention of hydrophilic phase, permeation of hydrophobic phase) would be expected if the (hydrophilic) membrane was replaced with a hydrophobic material.

The 3D-printed liquid-liquid separator (Fig. 4B–D) consisted of a single inlet leading to a spiral channel (semi-circular cross section, $\varnothing = 1.1$ mm, length = 895 mm) contacting the membrane. An identical spiral channel

mirrored this on the opposing side of the membrane and each spiral channel was connected to an outlet as shown in the computer generated 3D image, Fig. 4B, with the equivalent fabricated device shown in Fig. 4C. The incorporated membrane can be easily seen in the birds-eye view of the finished device in Fig. 3D. The membrane incorporation procedure followed the general protocol described for the syringe filter and devices were printed using both hydrophilic and hydrophobic membranes – mixed cellulose ester (MCE) and PTFE, respectively.

The separation efficiency was assessed using different flow rates (0.1–0.3 mL min⁻¹), whilst tuning the backpressure across the membrane by varying the length of a silica

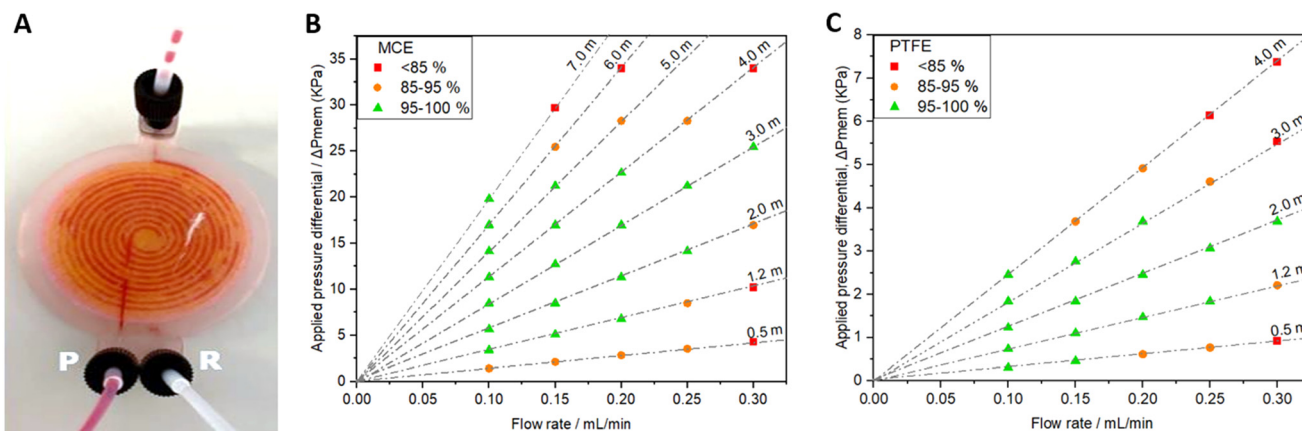


Fig. 5 A) Image of a liquid-liquid separator with a hydrophilic MCE membrane separating an incoming segmented flow (top) of FC-40 fluorinated oil and red-dyed water. The permeate and retentate outlets (bottom, labelled “P” and “R” respectively) show uniform colours indicating successful separation. B) and C) Separation efficiency of separators with MCE (B) and PTFE membranes (C) as a function of flow rate and backpressure. Dashed lines correspond to the different lengths of capillary used to apply the backpressure, with the lengths specified. Green data points indicate a separation of 95% or greater, orange points indicate a separation between 85 and 95%, while red data points represent poor separation (<85%).



capillary ($\varnothing = 0.56$ mm) on the retentate outlet. Careful control of the trans-membrane pressure is important^{32,33} – if insufficient to drive the permeate across the membrane some permeate will still be present in the retentate outlet, while if the pressure is increased above the capillary pressure, retentate fluid will be forced across the membrane and exit with the permeate. Images depicting these failure modes are shown in the ESI.† If the applied backpressure is between the permeate and capillary pressures, the fluids are fully separated. This is shown for example in Fig. 5A and the ESI† video. Both show successful separation of a segmented flow of FC-40 fluorinated oil and red-dyed water using a device with an MCE membrane. While the inlet clearly shows a segmented flow, the outlets (labelled “P” and “R” in Fig. 5A for permeate and retentate, respectively) show uniform colour indicating full separation.

The separation efficiencies across the tested flow range are shown in Fig. 5B and C for devices using MCE and PTFE membranes, respectively. In each case the applied pressure differential is calculated from the capillary dimensions using the Hagen–Poiseuille equation and separation was defined as the volumetric flow rate of liquid collected in the uniform (non-segmented) outlet stream relative to the expected volumetric flow rate (there will always be one uniform stream). Both the MCE and PTFE devices successfully separated the mixture within the flow rate range tested up to transmembrane pressures (ΔP_{mem}) of 25.5 kPa and 3.68 kPa, respectively. One key difference between the two devices was that during perfect separation the fluids exited the devices through opposite outlets (permeate *vs.* retentate) which is

consistent with hydrophilic membranes favouring permeation by hydrophilic fluids and *vice versa*. It is also important to note that the observed dependence of separation efficiency on flow rate and backpressure qualitatively matches the theoretical trends and those previously observed in a similar device,³⁴ consistent with expected behaviour.

Cross flow filtration

Cross flow filtration relies on the diffusion of a solute across a concentration gradient from a starting (donor) flow into an acceptor flow, as illustrated in Fig. 6A. The two flows (donor and acceptor) travel along a membrane in opposite directions to ensure a concentration gradient throughout the device which should, given sufficient time, allow complete transfer of solutes without any change in volumetric flow.

An initial prototype device was made with a similar design to the liquid–liquid separator, but with the addition of a further inlet to allow two independent flows either side of the membrane. In testing we found that the backpressure in the channel printed above the membrane was greater than that below the membrane, likely due to the over-extrusion used to seal the membrane reducing channel dimensions, which resulted in bulk fluid transport across the membrane. Hence a backpressure was applied at the exit port of the lower channel to compensate. This increase in pressure however had the unexpected effect of causing the device to expand below the membrane, causing separation of the membrane from the structures below it. Consequently, fluid

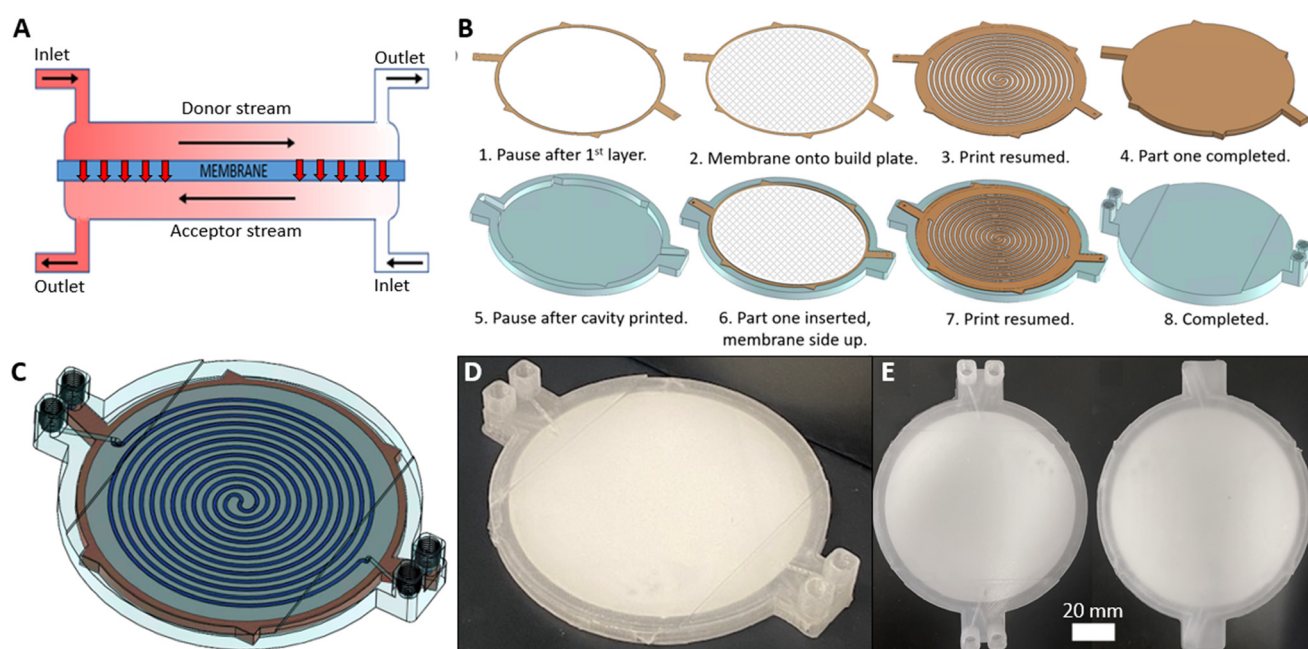


Fig. 6 A) Diagram illustrating the operation of the cross-flow filter, with the net movement of the dye (red arrows) from the donor to the acceptor stream. B) Process flow showing how the final device is built up in an 8-stage process. C) 3D computer generated image showing the final device with the membrane and channels above the membrane visible. D) Corresponding image of the fabricated device. E) Views of the device from above and below.



was free to travel along the most direct path from inlet to outlet rather than through the patterned channels, resulting in low residence times and poor dye removal. The expansion of the device below the membrane, with no expansion observed above, is consistent with the observation that while hot plastic extruded directly onto the membrane gave a conformal bond, there will be no such bond when the membrane is merely placed on top of a pre-existing printed structure. It should be noted that while the swelling of the volume below the membrane was not seen in the separator device, this is likely due to the smaller device size, much narrower and lower flow rate range, and hence lower pressures. The same effect would likely be seen when working at higher pressures.

To make a robust usable device it was therefore important that the membrane was bonded to the device on both sides. This could be achieved using an adhesive at all contact points,²⁸ however the addition of adhesive is subjective and challenging for reproducible fabrication. It also poses technical challenges due to potential wicking of the adhesive into the membrane. Hence a novel fabrication technique was developed whereby channels were directly patterned (and thus bonded) onto both sides of the membrane. This was achieved in a process shown in Fig. 6B, which involved two separate printing phases corresponding to the part areas shown in orange and blue.

The first phase started by printing an outline onto the print bed representing the membrane filter cavity (Fig. 6B-1). A pause after this first layer meant the membrane filter could be placed on the print bed (Fig. 6B-2) with a very small amount of a weak adhesive applied at the circumference to ensure it didn't move in the subsequent step. The print was resumed and a channel design directly patterned on the membrane surface (Fig. 6B-3) with additional layers sealing the channels (Fig. 6B-4). This part, which represented the channel network on one side of the membrane, was removed from the print bed and the second phase commenced by printing a hollow receptacle (Fig. 6B-5, blue) for the first part. Part one (orange) was placed within the receptacle (Fig. 6B-6) with the exposed membrane surface facing upwards and the print resumed. The channel design was once again printed directly onto the exposed surface (Fig. 6B-7) until full encapsulation and completion of the print (Fig. 6B-8) to yield the finished device (Fig. 6C-E).

During printing it was critical that the first component fitted within the cavity of the second such that the membrane was level with the print bed so that subsequent printing could proceed accurately, and that the channels were in the correct position for the next set of channels (- Fig. 6B-7) to be printed in the same relative position across the membrane. To achieve this a part height (Fig. 6B-4) and receptacle depth (Fig. 6B-5) of 3.9 mm and 4.0 mm respectively were used, while the *x,y*-dimensions of both the first component and receptacle void were identical. The channels above and below the membrane had an identical concentric pattern (length = 1042.9 mm) but differed slightly

in cross-section. The channels above the membrane (Fig. 6B-7) were slightly wider (1.24 mm *vs.* 1.0 mm) to allow for alignment imperfections. In both cases the channel height was the same (500 μm).

To test the device an aqueous solution of the organic dye methylene blue (0.01 mM) was flowed through the donor channel and deionised water through the bottom channel of the device in a counter current arrangement at varying flow rates (25–2000 $\mu\text{L min}^{-1}$ for each fluid) corresponding to residence times of 0.25 to 20.3 minutes. A micrometering valve was used at the outlet of the top channel cavity and manually tuned to ensure equal flow rates at the device outlets. Both the donor and acceptor fluid were collected at the outlet and analysed *via* absorbance spectroscopy to determine dye concentration.

The device performed as expected: as the residence time was increased (0.25–2.54 min) there was a steep linear increase in dye removal before plateauing after 3.4 min at near full dye removal (98.2%) (Fig. 7). The diffusion coefficient for methylene blue has been reported as $6.74 \times 10^{-6} \text{ cm}^2 \text{ s}^{-1}$.³⁵ Using this value and the nominal channel dimensions a theoretical residence time for 100% removal was calculated as 3.09 minutes – in good agreement with the experimental findings. Beyond this point, dye removal varied slightly around 98.2% and did not achieve 100% removal, highlighting the difference of experimental to theoretical values and likely a result of the random motion of dye molecules, a characteristic assumed negligible within Fick's law.

The results show the cross-flow filtration device to be highly effective, and did not encounter any of the problems experienced in the earlier prototypes, even at the highest flow rates. This is consistent with the successful bond between the membrane and the device body using our novel double-sided printing approach. As for all the devices reported in this work, there is large scope for customisability, both in

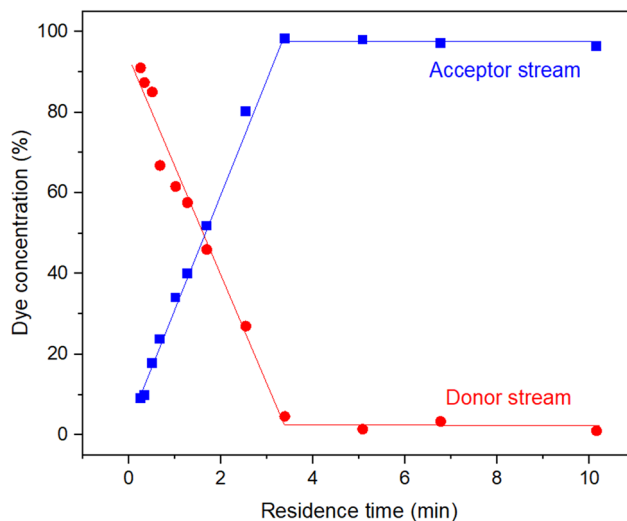


Fig. 7 Experimental data for the removal of methylene blue from an aqueous flow (0.01 mM) using the cross-flow filtration device.



terms of the 3D printed structure but also the membrane material and size.

Conclusion

In conclusion, we have shown how commercial porous membranes can be incorporated into FDM 3D printed fluidic devices using the print–pause–print technique to make functional separation devices. This is the first time that fully-functional, membrane-containing devices have been fabricated using 3D printing without needing subsequent post-printing assembly. The versatility of this approach is shown by the fact that we have shown three distinct devices, with three different functionalities and that these can be arbitrarily customised and tailored depending on end user requirements. We have shown a new approach to print on both sides of the membrane for instances where it is important that printed structures are firmly attached to both sides of the membrane. While the three device-types showcased here give examples of the type of device that can be made when incorporating membranes into 3D printed structures, there are numerous other types of chemical processing equipment and chemical reactors that could exploit the same approach; for example, applying to reactor technology for combined synthesis and workup in a single device, or as a route for addition or removal of gases during a reaction. The versatility of 3D printing and the increasing maturity of 3D printing technology, means that the incorporation of membranes *via* PPP will be an enduring tool for fabrication of fluidic devices – not only for separation and filtration, but for chemical processing devices more generally.

Conflicts of interest

The authors have no conflicts to declare.

Acknowledgements

AMN is supported by the Natural Environment Research Council *via* an Industrial Innovation Fellowship (NE/R013578/1) and the Signals in the Soil program (NE/T010584/1). MJC's PhD research is supported by the University of Southampton's Faculty of Engineering and Physical Sciences *via* the Centre of Excellence for Continuous Digital Chemical Engineering Science. CT scanning was supported by the National Research Facility for Lab X-ray CT (NXCT) at the μ -VIS X-ray Imaging Centre, University of Southampton, through EPSRC grant EP/T02593X/1.

References

- 1 F. Li, N. P. MacDonald, R. M. Guijt and M. C. Breadmore, Multimaterial 3D Printed Fluidic Device for Measuring Pharmaceuticals in Biological Fluids, *Anal. Chem.*, 2019, **91**(3), 1758–1763, DOI: [10.1021/acs.analchem.8b03772](https://doi.org/10.1021/acs.analchem.8b03772).
- 2 H. K. Balakrishnan, E. H. Doeven, A. Merenda, L. F. Dumée and R. M. Guijt, 3D printing for the integration of porous materials into miniaturised fluidic devices: A review, *Anal. Chim. Acta*, 2021, 1185, DOI: [10.1016/j.aca.2021.338796](https://doi.org/10.1016/j.aca.2021.338796).
- 3 P. J. Kitson, M. H. Rosnes, V. Sans, V. Dragone and L. Cronin, Configurable 3D-Printed millifluidic and microfluidic “lab on a chip” reactionware devices, *Lab Chip*, 2012, **12**(18), 3267–3271, DOI: [10.1039/c2lc40761b](https://doi.org/10.1039/c2lc40761b).
- 4 F. Lederle, F. Meyer, C. Kaldun, J. C. Namyslo and E. G. Hübner, Sonogashira coupling in 3D-printed NMR cuvettes: synthesis and properties of aryl naphthylalkynes, *New J. Chem.*, 2017, **41**(5), 1925–1932, DOI: [10.1039/c6nj03614g](https://doi.org/10.1039/c6nj03614g).
- 5 M. Oellers, F. Lucklum and M. J. Vellekoop, On-chip mixing of liquids with swap structures written by two-photon polymerization, *Microfluid. Nanofluid.*, 2020, **24**(1), 1–8, DOI: [10.1007/s10404-019-2309-8](https://doi.org/10.1007/s10404-019-2309-8).
- 6 C. W. Pinger, A. A. Heller and D. M. Spence, A Printed Equilibrium Dialysis Device with Integrated Membranes for Improved Binding Affinity Measurements, *Anal. Chem.*, 2017, **89**(14), 7302–7306, DOI: [10.1021/acs.analchem.7b01848](https://doi.org/10.1021/acs.analchem.7b01848).
- 7 G. Scotti, S. M. E. Nilsson and M. Haapala, *et al.*, A miniaturised 3D printed polypropylene reactor for online reaction analysis by mass spectrometry, *React. Chem. Eng.*, 2017, **2**(3), 299–303, DOI: [10.1039/c7re00015d](https://doi.org/10.1039/c7re00015d).
- 8 F. Li, M. R. Ceballos and S. K. Balavandy, *et al.*, 3D Printing in analytical sample preparation, *J. Sep. Sci.*, 2020, **43**(9–10), 1854–1866, DOI: [10.1002/jssc.202000035](https://doi.org/10.1002/jssc.202000035).
- 9 U. Kalsoom, P. N. Nesterenko and B. Paull, Current and future impact of 3D printing on the separation sciences, *TrAC, Trends Anal. Chem.*, 2018, **105**, 492–502, DOI: [10.1016/j.trac.2018.06.006](https://doi.org/10.1016/j.trac.2018.06.006).
- 10 D. J. Cocovi-Solberg, P. J. Worsfold and M. Miró, Opportunities for 3D printed millifluidic platforms incorporating on-line sample handling and separation, *TrAC, Trends Anal. Chem.*, 2018, **108**, 13–22, DOI: [10.1016/j.trac.2018.08.007](https://doi.org/10.1016/j.trac.2018.08.007).
- 11 C. Echaide-Górriz, C. Clément, F. Cacho-Bailo, C. Téllez and J. Coronas, New strategies based on microfluidics for the synthesis of metal-organic frameworks and their membranes, *J. Mater. Chem. A*, 2018, **6**(14), 5485–5506, DOI: [10.1039/c8ta01232f](https://doi.org/10.1039/c8ta01232f).
- 12 T. Monaghan, M. J. Harding, R. A. Harris, R. J. Friel and S. D. R. Christie, Customisable 3D printed microfluidics for integrated analysis and optimisation, *Lab Chip*, 2016, **16**(17), 3362–3373, DOI: [10.1039/c6lc00562d](https://doi.org/10.1039/c6lc00562d).
- 13 J. M. Zhang, E. Q. Li, A. A. Aguirre-Pablo and S. T. Thoroddsen, A simple and low-cost fully 3D-printed non-planar emulsion generator, *RSC Adv.*, 2016, **6**(4), 2793–2799, DOI: [10.1039/c5ra23129a](https://doi.org/10.1039/c5ra23129a).
- 14 G. W. Bishop, J. E. Satterwhite-Warden, I. Bist, E. Chen and J. F. Rusling, Electrochemiluminescence at Bare and DNA-Coated Graphite Electrodes in 3D-Printed Fluidic Devices, *ACS Sens.*, 2016, **1**(2), 197–202, DOI: [10.1021/acssensors.5b00156](https://doi.org/10.1021/acssensors.5b00156).
- 15 A. D. Castiaux, C. W. Pinger, E. A. Hayter, M. E. Bunn, R. S. Martin and D. M. Spence, PolyJet 3D-Printed Enclosed Microfluidic Channels without Photocurable Supports, *Anal.*



- Chem.*, 2019, **91**(10), 6910–6917, DOI: [10.1021/acs.analchem.9b01302](https://doi.org/10.1021/acs.analchem.9b01302).
- 16 S. J. Keating, M. I. Gariboldi, W. G. Patrick, S. Sharma, D. S. Kong and N. Oxman, 3D printed multimaterial microfluidic valve, *PLoS One*, 2016, **11**(8), 1–12, DOI: [10.1371/journal.pone.0160624](https://doi.org/10.1371/journal.pone.0160624).
- 17 F. Li, N. P. Macdonald, R. M. Guijt and M. C. Breadmore, Increasing the functionalities of 3D printed microchemical devices by single material, multimaterial, and print-pause-print 3D printing, *Lab Chip*, 2019, **19**(1), 35–49, DOI: [10.1039/c8lc00826d](https://doi.org/10.1039/c8lc00826d).
- 18 Y. T. Kim, A. Ahmadianyazdi and A. Folch, 'print - pause - print' protocol for 3D printing microfluidics using multimaterial stereolithography, *Nat. Protoc.*, 2023, **18**, 1243–1259, DOI: [10.1038/s41596-022-00792-6](https://doi.org/10.1038/s41596-022-00792-6).
- 19 M. R. Penny, N. Tsui and S. T. Hilton, Extending practical flow chemistry into the undergraduate curriculum via the use of a portable low-cost 3D printed continuous flow system, *J. Flow Chem.*, 2021, **11**(1), 19–29, DOI: [10.1007/s41981-020-00122-5](https://doi.org/10.1007/s41981-020-00122-5).
- 20 G. Gaal, M. Mendes and T. P. de Almeida, *et al.*, Simplified fabrication of integrated microfluidic devices using fused deposition modeling 3D printing, *Sens. Actuators, B*, 2017, **242**, 35–40, DOI: [10.1016/j.snb.2016.10.110](https://doi.org/10.1016/j.snb.2016.10.110).
- 21 G. I. J. Salentijn, P. E. Oomen, M. Grajewski and E. Verpoorte, Fused Deposition Modeling 3D Printing for (Bio) analytical Device Fabrication: Procedures, *Anal. Chem.*, 2017, **89**(13), 7053–7061, DOI: [10.1021/acs.analchem.7b00828](https://doi.org/10.1021/acs.analchem.7b00828).
- 22 M. Banna, K. Bera and R. Sochol, *et al.*, 3D printing-based integrated water quality sensing system, *Sensors*, 2017, **17**(6), 1336, DOI: [10.3390/s17061336](https://doi.org/10.3390/s17061336).
- 23 P. F. Flowers, C. Reyes, S. Ye, M. J. Kim and B. J. Wiley, 3D printing electronic components and circuits with conductive thermoplastic filament, *Addit. Manuf.*, 2017, **2020**(18), 156–163, DOI: [10.1016/j.addma.2017.10.002](https://doi.org/10.1016/j.addma.2017.10.002).
- 24 E. Aguilera, J. Ramos, D. Espalin and F. Cedillos, *3D Printing of Electro Mechanical Systems*, 2013, pp. 950–961.
- 25 A. D. Castiaux, C. W. Pinger and D. M. Spence, Ultrafiltration binding analyses of glycated albumin with a 3D-printed syringe attachment, *Anal. Bioanal. Chem.*, 2018, **410**(29), 7565–7573, DOI: [10.1007/s00216-018-1373-3](https://doi.org/10.1007/s00216-018-1373-3).
- 26 R. Tan and M. Franzreb, Continuous ultrafiltration/diafiltration using a 3D-printed two membrane single pass module, *Biotechnol. Bioeng.*, 2020, **117**(3), 654–661, DOI: [10.1002/bit.27233](https://doi.org/10.1002/bit.27233).
- 27 F. Li, P. Smejkal, N. P. Macdonald, R. M. Guijt and M. C. Breadmore, One-Step Fabrication of a Microfluidic Device with an Integrated Membrane and Embedded Reagents by Multimaterial 3D Printing, *Anal. Chem.*, 2017, **89**(8), 4701–4707, DOI: [10.1021/acs.analchem.7b00409](https://doi.org/10.1021/acs.analchem.7b00409).
- 28 P. K. Yuen, Embedding objects during 3D printing to add new functionalities, *Biomicrofluidics*, 2016, **10**(4), 044104, DOI: [10.1063/1.4958909](https://doi.org/10.1063/1.4958909).
- 29 Y. R. Lee, M. S. Jang, H. Y. Cho, H. J. Kwon, S. Kim and W. S. Ahn, ZIF-8: A comparison of synthesis methods, *Chem. Eng. J.*, 2015, **271**, 276–280, DOI: [10.1016/j.cej.2015.02.094](https://doi.org/10.1016/j.cej.2015.02.094).
- 30 A. Zargaryan, N. Farhoudi, G. Haworth, J. F. Ashby and S. H. Au, Hybrid 3D printed-paper microfluidics, *Sci. Rep.*, 2020, **10**(1), 1–9, DOI: [10.1038/s41598-020-75489-5](https://doi.org/10.1038/s41598-020-75489-5).
- 31 R. M. Dirkzwager, S. Liang and J. A. Tanner, Development of Aptamer-Based Point-of-Care Diagnostic Devices for Malaria Using Three-Dimensional Printing Rapid Prototyping, *ACS Sens.*, 2016, **1**(4), 420–426, DOI: [10.1021/acssensors.5b00175](https://doi.org/10.1021/acssensors.5b00175).
- 32 A. Adamo, P. L. Heider, N. Weeranoppanant and K. F. Jensen, Membrane-Based, Liquid - Liquid Separator with Integrated Pressure Control, *Ind. Eng. Chem. Res.*, 2013, **52**(31), 10802–10808, DOI: [10.1021/ie401180t](https://doi.org/10.1021/ie401180t).
- 33 T. W. Phillips, J. H. Bannock and J. C. deMello, Microscale extraction and phase separation using a porous capillary, *Lab Chip*, 2015, **15**, 2960–2967, DOI: [10.1039/c5lc00430f](https://doi.org/10.1039/c5lc00430f).
- 34 O. K. Castell, C. J. Allender and D. A. Barrow, Liquid-liquid phase separation: Characterisation of a novel device capable of separating particle carrying multiphase flows, *Lab Chip*, 2009, **9**(3), 388–396, DOI: [10.1039/b806946h](https://doi.org/10.1039/b806946h).
- 35 A. A. Selifonov, O. G. Shapoval, A. N. Mikerov and V. V. Tuchin, Determination of the Diffusion Coefficient of Methylene Blue Solutions in Dentin of a Human Tooth using Reflectance Spectroscopy and Their Antibacterial Activity during Laser Exposure, *Opt. Spectrosc.*, 2019, **126**(6), 758–768, DOI: [10.1134/S0030400X19060213](https://doi.org/10.1134/S0030400X19060213).

